Journal of
Materials Chemistry A

Accepted Manuscript

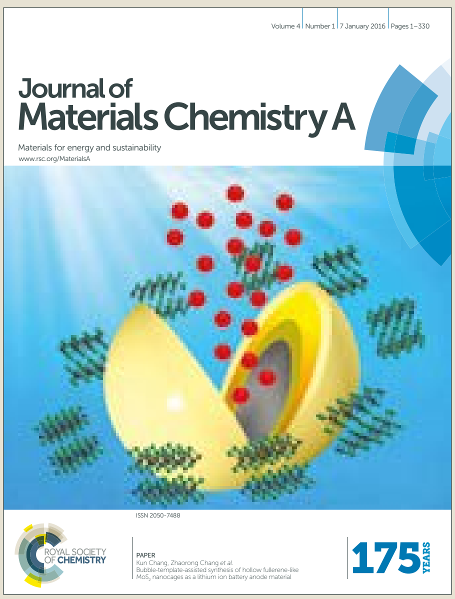

View Article Online
DOI: 10.1039/C8TA10510C

Room-Temperature-Processing Fullerene Single-Crystalline Nanoparticles for High-Performance Flexible Perovskite Photovoltaics

Xiaoming Zhao[1,4,5,#], Lixian Tian[2,4], Tianjun Liu[3,5], Hongli Liu[1,4,], Shirong Wang[1,4,*], Xianggao Li[1,4], Oliver Fenwick[3,5], Shengbin Lei[2,4] and Wenping Hu[2,4]*

[1] School of Chemical Engineering and Technology, Tianjin University, Tianjin 300354, China.

[2] Department of Chemistry, Tianjin Key Laboratory of Molecular Optoelectronic Science, School of Science, Tianjin University, Tianjin 300072, China

[3] School of Engineering and Materials Science, Queen Mary University of London, 327 Mile End Road, London E1 4NS, United Kingdom.

[4] Collaborative Innovation Center of Chemical Science and Engineering (Tianjin), Tianjin 300072, China.

[5] Materials Research Institute, Queen Mary University of London, 327 Mile End Road, London E1 4NS, United Kingdom

*Corresponding Authors: liuhongli@tju.edu.cn (Hongli Liu); wangshirong@tju.edu.cn (Shirong Wang)

Present Address: Department of Chemical and Biological Engineering, Princeton University, Princeton, New Jersey 08544, United States

KEYWORDS: fullerene nanoparticles; single crystal; organic scaffold; perovskite solar cells.

View Article Online
DOI: 10.1039/C8TA10510C

ABSTRACT: Organic-inorganic hybrid perovskite solar cells (PSCs) employing a mesoporous metal-oxide scaffold are now at the forefront of solution-processing photovoltaic cells, yielding a power conversion efficiency exceeding 23%. However, processing temperatures of up to 450 ℃ are typically required to sinter the mesoporous metal-oxide scaffolds, which hinders the fabrication of low-cost and flexible devices. Moreover, these metal-oxide scaffolds usually suffer from high charge carrier recombination rates and inherent UV instability. In this paper, we develop for the first time an organic-scaffold architecture, which consists of room-temperature-processing C_{60} single-crystalline nanoparticles (C_{60}-NPs) serving as an electron selective contact covering on C_{60} compact films (c-C_{60}). C_{60}-NPs act as a three-dimensional framework to support perovskite crystals, enabling it to cover the substrate more uniformly and thus demonstrating an advantage over planar heterojunction PSCs. Furthermore, the higher electron mobility of C_{60}-NPs compared with commonly-used TiO_2 enhances the charge transfer from perovskite to electron transport layers and reduces charge carrier accumulation at the interface, demonstrating the advantage of an organic scaffold over inorganic metal-oxide for mesoporous scaffold PSCs. A power conversion efficiency (PCE) of 19.45% was obtained in organic-scaffold $MAPbI_3$-based perovskite solar cells (OPSCs), outperforming standard reference devices based on a TiO_2 mesoporous scaffold (maximum PCE = 17.07%). Furthermore, the high UV stability of C_{60}-NPs enables the realisation of ultra-stable OPSCs stressed in ambient conditions and working under both UV and full-sun illumination. Moreover, the devices can be easily processed under low temperatures, providing an efficient method for the large-scale

View Article Online
DOI: 10.1039/C8TA10510C

production of flexible PSCs. These flexible PSCs show remarkable performance with an excellent PCE of 17.28 %, which is among the highest values reported for $MAPbI_3$-based flexible PSCs to date. This work reveals that organic nanostructures as n-type charge collection layers are ideal replacements for the inorganic mesoporous scaffold as they achieve remarkably high efficiency and long-term operational stability in both rigid and flexible perovskite solar cells.

View Article Online
DOI: 10.1039/C8TA10510C

Organic-inorganic hybrid perovskite solar cells (PSCs) have made impressive advancement since they were first discovered in 2009, and their power conversion efficiency (PCE) has developed from 3.81 to 23.2% by means of solvent engineering, interface engineering, and composition engineering, which comes close to the performance of polycrystalline silicon photovoltaics.[1–12] Two dominant device architectures, namely planar heterojunction and mesoporous scaffold structures, have been developed.[13–16] The planar heterojunction PSCs are either fabricated layer by layer *via* high-vacuum deposition or the solution-based method.[5,16,17] However, the high-vacuum deposition method requires complex equipment and consumes energy, while the formation of homogeneous film using the low-cost solution-processing method is difficult due to the dewetting process and sensitivity to the atmosphere.[17–19] Because of these limitations, most efficient devices still employ a mesoscopic TiO_2 scaffold as an electron-selective layer despite the significant progress made on planar PSCs.[20–24] However, the preparation of inorganic metal oxide nanostructures as a mesoporous scaffold is complex and requires sintering at a high temperature of > 450 ℃, which makes them unsuitable for flexible PSCs.[25] Therefore, the development of a low-temperature-processing electron-selective scaffold is urgently needed.

Fullerene and its derivatives are among the most widely-used n-type materials in organic electronic devices as they have both a suitable energy level alignment and superior electron mobility.[26–29] Furthermore, fullerene materials can be easily processed into single-crystalline nanostructures at room temperature, such as zero-dimensional nanoparticles, one-dimensional nanowires, and two-dimensional nanoribbons.[30–35]

View Article Online
DOI: 10.1039/C8TA10510C

Therefore, developing fullerene nanostructures as a room-temperature-processing organic electron-selective scaffold would constitute a significant development for PSCs. In this paper, we report a novel perovskite solar cell architecture based on a single-crystalline C_{60} nanoparticles (C_{60}-NPs) scaffold. The single-crystalline C_{60}-NPs is simply prepared at room temperature and is then deposited by spin-coating onto a C_{60} compact layer (c-C_{60}) to form the organic scaffold. As a three-dimensional skeleton, C_{60}-NPs improve the wettability between the C_{60} compact layer and the precursor for the $CH_3NH_3PbI_3$ ($MAPbI_3$) film, thereby enabling perovskite crystals to cover the substrate more uniformly and decrease the defect concentration of perovskite film. Moreover, compared to the conventionally-used electron-transport architecture – the compact TiO_2 layer/mesoporous TiO_2 scaffold (c-TiO_2/m-TiO_2), the proposed organic scaffold architecture enhances electron extraction and transport and reduces charge accumulation at the interface. The organic-scaffold $MAPbI_3$-based perovskite solar cells (OPSCs) achieved an average PCE of (18.41 ± 0.54) %, a value significantly higher than standard reference PSCs based on c-TiO_2/m-TiO_2 (maximum PCE = 17.07 %). Furthermore, due to the high UV stability of C_{60}-NPs, this approach facilitates the realisation of ultra-stable PSCs that are stressed in ambient conditions and work under both UV and one-sun illumination. Notably, OPSCs retain 80% of their initial performance after 720 h of continuous stress testing in ambient conditions under one-sun illumination at continuous maximum power, thus approaching the standards required for industrial stability. Most importantly of all, the devices can be easily processed under low temperatures, offering an efficient method for the large-scale

View Article Online
DOI: 10.1039/C8TA10510C

production of flexible PSCs. These flexible PSCs exhibit remarkable performance with an excellent PCE of 17.28 % and good mechanical tolerance, which is among the highest values reported for flexible PSCs to date.

The C_{60}-NPs were formed in a solvent mixture of toluene and ethanol, following the method described by Andrievsky *et al*.[36,37] The nanoparticles that we obtained were then filtered and moved into vigorously stirred ethanol and a highly concentrated dispersion containing 5 mg mL^{-1} of C_{60}-NPs was then prepared. Finally, the as-prepared C_{60}-NPs dispersion was spin-coated onto a thermally deposited C_{60} compact layer to form the organic scaffold architecture. Further details regarding preparation can be found in the **Experimental Section** (Supporting Information). It is important to note that the whole preparation process was conducted at room temperature without any thermal treatment.

To characterise the morphology of as-prepared nanoparticles, the atomic force microscope (AFM) and transmission electron microscope (TEM) images in **Figure 1a and b** were presented to show that the C_{60} particles used are very uniform. As shown in the distribution curve in **Figure S1** (Supporting Information), The average sizes of the nanoparticles were calculated to be (76.22 ± 18.40) nm by measuring the diameter of 200 nanoparticles. High-resolution transmission electron microscopy (HRTEM) results (**Figure 1c**) indicate that the as-prepared C_{60} nanoparticles are crystalline and the marked periodicity 0.803 nm corresponds to the spacing distance of the (111) plane. The selected area electron diffraction (SAED) pattern of individual C_{60}-NP is shown in **Figure 1d**. The presence of discrete diffraction points in the SAED patterns was

View Article Online
DOI: 10.1039/C8TA10510C

observed, indicating single crystallinity of the nanoparticle. The XRD patterns of the C_{60}-NPs (**Figure 1e**) can be indexed with a face-centred cubic (FCC) crystal system, where it is notable that the (200) reflection is missing. The extinction of the (200) reflection is typical of pristine FCC C_{60} crystals.[38] The lattice constant of the C_{60}-NPs is a = 1.413 nm, which consists well with the 1.415 nm value of pristine C_{60} crystals.[39] We have previously reported that the highly-ordered molecular organisation of organic single crystals can remarkably enhance their charge transport properties.[33] Therefore, the single-crystalline nature of as-prepared C_{60}-NPs is beneficial for charge transfer when using them as a charge transport layer, which may also significantly reduce charge accumulation at the interfaces. Spin-coating C_{60}-NPs dispersion onto a C_{60} compact layer can form a dense, pinhole-free film (**Figure 1f**). Additionally, the c-C_{60}/C_{60}-NPs that were prepared showed enhanced transmittance in the visible region compared to c-TiO_2/m-TiO_2 (**Figure S2**, Supporting Information). This high transparency can effectively avoid the parasitic absorption of the perovskite absorber to maximize the resultant photocurrent of the relevant PSCs.[40]

As shown in **Figure 2a-c**, the organic-scaffold architecture inherits the basic structure of PSCs with an inorganic mesoporous scaffold.[13–15] In this architecture, the inorganic nanocrystal scaffolds are replaced with organic C_{60}-NPs networks that can be processed at room temperature, as noted previously. The fabrication of organic-scaffold perovskite solar cells (OPSCs), which is included in details in the **Experimental Section** (supporting information), is similar to that of PSCs based on an inorganic mesoporous scaffold. The surface wettability of the contacted film is important for the

View Article Online
DOI: 10.1039/C8TA10510C

formation of a high-quality $MAPbI_3$ film.[28] The dewetting of C_{60} compact thin films can result in $MAPbI_3$ film with incomplete coverage and a non-uniform film after solution-processing and subsequent baking.[41,42] According to the literature, the dewetting of thin films becomes completely suppressed following the addition of a small amount of C_{60}-NPs, which stabilises the film by apparent pinning.[42–45] Therefore, the employment of C_{60}-NPs in this experiment may improve the wettability between the C_{60} compact film and the precursor solution for the perovskite film. To study the effect of C_{60}-NPs on surface wettability, we measured the contact angles of $MAPbI_3$ precursor solution on different surfaces. As shown in **Figures 2d and e**, the contact angle of $MAPbI_3$ precursor solution on the C_{60} compact film was 62.7°, which is much larger compared to C_{60} films covered with C_{60}-NPs (16.1°). Thus, the wettability between the C_{60} compact film and the perovskite precursor solution can be significantly improved by C_{60}-NPs, which may facilitate the spreading of the perovskite precursor solutions and the formation of high-quality $MAPbI_3$ films. For comparison, we also examined the wettability of c-TiO_2/m-TiO_2 film in which the perovskite precursor has a contact of 38.5°, a value significantly higher than that for an organic scaffold (c-C_{60}/C_{60}-NPs). Therefore, it was expected that higher-quality perovskite films can be formed on an organic scaffold (c-C_{60}/C_{60}-NPs) than on an inorganic scaffold (c-TiO_2/m-TiO_2). To verify this hypothesis, SEM observation was carried out. **Figures 2g and h** present top-view SEM images of the perovskite films with and without an organic scaffold. Perovskite films without a scaffold display pinholes and bare substrates, raising the risk of short circuits. By contrast, perovskite films on a scaffold shown

View Article Online
DOI: 10.1039/C8TA10510C

continuous and complete coverage, demonstrating an advantage above planar heterojunction PSCs. Furthermore, uniformly spread organic scaffolds work as TiO_2 scaffolds but, compared to perovskite films on TiO_2 scaffolds, can also support perovskite crystal growth with larger grain sizes of up to several micrometres (**Figure 2h and i**). Moreover, organic scaffolds can be prepared in a less costly and much simpler way, which further demonstrates the advantage of an organic scaffold over an inorganic mesoporous scaffold for perovskite solar cells.

To compare the charge generation efficiency, we measured the optical absorption of $MAPbI_3$ films on an organic scaffold and an inorganic mesoporous scaffold, the data for which are displayed in **Figure 3a**. The absorption intensity of $MAPbI_3$ film on an organic scaffold (c-C_{60}/C_{60}-NPs) is a little stronger than that on an inorganic mesoporous scaffold (c-TiO_2/m-TiO_2). This may be due to the larger perovskite grains.

In addition to the efficiency of charge generation, charge-carrier mobility also affects the performance of the device. Low mobility of the electron transport layer (ETL) indicates more traps and will slow down charge transport. This could lead to charge accumulation at the interface, which will induce an energy barrier to suppress the charge transport.[46] To compare the charge transport properties in the organic and inorganic scaffolds, we measured the mobility of c-C_{60}/C_{60}-NPs and c-TiO_2/m-TiO_2 films following the space-charge-limited-current (SCLC) method,[47] the results of which are presented in **Figure 3b**. The mobility of the c-C_{60}/C_{60}-NPs film was found to be approximately 1.2×10^{-2} cm^2 V^{-1} s^{-1}, which is much higher than that of c-TiO_2/m-TiO_2

View Article Online
DOI: 10.1039/C8TA10510C

(4.2×10^{-5} cm^2 V^{-1} s^{-1}). This indicates that, compared to c-TiO_2/m-TiO_2 architecture, c-C_{60}/C_{60}-NPs architecture can offer more rapid charge transport through the ETLs.

The interfacial charge transfer process plays vital role in the charge recombination and device efficiency.[8] To understand the charge transfer process in PSCs, the steady-state photoluminescence (PL) and time-resolved photoluminescence (TRPL) spectra were collected to reveal the charge transport behavior at the interface of ETL/perovskite.[48,49] **Figure 3c** shows the PL spectra of perovskite, c-TiO_2/m-TiO_2/perovskite and c-C_{60}/C_{60}-NPs/perovskite. The spectra of the perovskite films all showed an emission peak of ~770 nm, which is typical of $MAPbI_3$, but in each case the intensity of the peak was substantially less than that of the peak for $MAPbI_3$ on glass. It is clear that both c-C_{60}/C_{60}-NPs and c-TiO_2/m-TiO_2 underlayers quenched the perovskite emission, and the c-C_{60}/C_{60}-NPs underlayer exihited stronger quenching compared to the c-TiO_2/m-TiO_2 underlayer. This indicates that c-C_{60}/C_{60}-NPs allowed more efficient electron extraction and transport from perovskite to the ETLs. Moreover, we investigated the TRPL lifestimes for perovskites on ITO, ITO/c-C_{60}/C_{60}-NPs, and ITO/c-TiO_2/m-TiO_2. As shown in **Figure 4d**, The TRPL plots were fitted *via* a biexponential Equation (1)

$$f(t) = A_1\exp(-t/\tau_1) + A_2\exp(-t/\tau_2) + B \qquad (1)$$

where τ_1 and τ_2 are slow and fast decay time constants, respectively, A_1 and A_2 are their corresponding decay amplitudes, and B is a constant.[50] For the $MAPbI_3$ sample, the τ_1 and τ_2 were 69.32 and 12.79 ns, respectively. When the inorganic mesoporous scaffold c-TiO_2/m-TiO_2 was introduced, the τ_1 and τ_2 both decreased to 48.10 and 8.70

View Article Online
DOI: 10.1039/C8TA10510C

ns, respectively. When the organic scaffold c-C_{60}/C_{60}-NPs was introduced, the τ_1 and τ_2 decreased further to 43.84 and 3.79 ns, respectively. Apparently, the perovskite/organic scaffold system can provide a faster electron transfer process and lower interface recombination in compared with the perovskite/inorganic mesoporous scaffold system. Therefore, the charge transportation and injection get improved and less charge accumulation occurs at the interface of ETL/perovskite, thus leading to the reduced hysteresis behavior in the device with organic scaffold, as discussed in the following section.[20,28,51] Moreover, electrochemical impedance spectroscopy (EIS) was also employed to investigate the interfacial carrier transfer and recombination kinetics in PSCs.[8] **Figure S3a** shows the Nyquist plots measured in dark condition with the equivalent circuit in the inset for the devices with the c-TiO_2/m-TiO_2 and c-C_{60}/C_{60}-NPs ETLs, respectively. The high frequency semicircle is attributed to the transport resistance (R_{tr}), whereas the low frequency part is determined by the recombination resistance (R_{rec}).[52] Due to the simplified transmission line model, the high frequency semicircle is almost indistinguishable and the Nyquist plots in **Figure S3a,** showing a main semicircle at low frequency, is according to the recombination processes. As shown in **Figure S3b**, the recombination resistance is closely related with the applied bias with the fitted R_{rec} values of the organic scaffold devices much higher compared with inorganic scaffold devices. Therefore, the organic scaffold devices can inhibit the charge carriers recommendation and improve the interfacial charge transfer.

Figure S4 (supporting information) shows the typical device structre of the n-i-p perovskite solar cell which consists of Gold/Spiro-OMeTAD/$MAPbI_3$/m-TiO_2/c-

View Article Online
DOI: 10.1039/C8TA10510C

TiO_2/fluorine doped tin oxide (FTO)/glass. This device served as a control device for comparison. To examine the performance of the c-C_{60}/C_{60}-NPs organic scaffold, we fabricated OPSCs by replacing the TiO_2 compact and mesoporous layers with the C_{60} compact layer and C_{60}-NPs. For OPSCs based on an organic scaffold, the ETL formation did not need the high-temperature processing. Therefore, an indium-tin oxide (ITO) electrode with higher transmittance than the FTO electrode in a visible range was utilised as a cathode on a glass substrate. A C_{60} compact layer with a thickness of 10 nm was deposited on the ITO/glass substrate using thermal evaporation in a vacuum environment upon which C_{60}-NPs were then spin-coated as an organic scaffold. The $MAPbI_3$ was then deposited onto the C_{60}-NPs scaffold and the hole transport material Spiro-OMeTAD was spin-coated on top of the $MAPbI_3$ layer. Lastly, the anode, Gold, was thermally evaporated to finalise the device fabrication. Further details concerning device fabrication can be found in the **Experimental Section** (Supporting Information). A schematic diagram and cross-sectional SEM image of the final device are displayed as **Figures 4a and b**.

Figure 4c depicts the typical *J-V* characteristics of the champion devices based on c-C_{60}/C_{60}-NPs and c-TiO_2/m-TiO_2 under AM 1.5 G illumination. The average values and standard deviations of key photovoltaic parameters are summarised in **Table 1**. Firstly, we investigated the effect of the thickness of C_{60}-NPs on photovoltaic performance of perovskite solar cells. **Figure S5a** shows dependence of PCE (measured from reverse scan) on C_{60}-NPs thickness. As shown in **Figure S5b-e**, in absence of C_{60}-NPs, *i. e.* when the thickness of C_{60}-NPs is 0 nm, the cells gave relatively lower open-

View Article Online
DOI: 10.1039/C8TA10510C

circuit voltage (V_{OC}), short-circuit photocurrent density (J_{SC}) and fill factor (FF) compared to the cells employing C_{60}-NPs. This is due to the lower-quality perovskite crystals formed directly on C_{60} compact layer and the relatively poor electron collection ability of C_{60} compact layer due to small contact surface. When employing C_{60}-NPs as organic scaffold, PCE changed mainly due to change of FF as shown in **Figure S5**. The optimum thickness of C_{60}-NPs that exhibited the highest PCE at 19.45% was determined to be 50 nm. PCE decreased as the C_{60}-NPs thickness increased over 50 nm. This was due to decreased conductivity of thick C_{60}-NPs that increased the series resistance of the device and resulted in lower FF (**Figures S5d, e**). PCE also decreased as the C_{60}-NPs thickness decreased below 50 nm. Considering that the C_{60}-NPs has a particle size from 40 to 100 nm, this performance reduction was possibly due to pinholes or tunneling recombination on the thinnest C_{60}-NPs layer. When applying the optimized C_{60}-NPs thickness, the PSC based on c-C_{60}/C_{60}-NPs yielded the highest PCE of 19.45% with a V_{OC} of 1.08 V, a J_{SC} of 22.79 mA cm^{-2}, and an FF of 0.79, clearly outperforming the PSCs based on c-TiO_2/m-TiO_2 ETLs. The best-performing reference cell using c-TiO_2/m-TiO_2 ETLs gave a J_{SC} of 22.10 mA cm^{-2}, V_{OC} of 0.99 V, FF of 0.78, and PCE of 17.07%. These values are comparable with those of a previous report on devices with the same structure.[53] The improved photovoltaic performances of the c-C_{60}/C_{60}-NPs devices can be attributed to the following causes: 1) the high electron mobility of c-C_{60}/C_{60}-NPs facilitated electron extraction and transport from perovskite to the ETLs, effectively hindering charge recombination at the ETL/perovskite interface; 2) C_{60}-NPs well supported the perovskite active layer which has large grains

View Article Online
DOI: 10.1039/C8TA10510C

and fewer grain boundaries; 3) The uniform $MAPbI_3$ films formed on the c-C_{60}/C_{60}-NPs substrate improved interfacial contact between the $MAPbI_3$ layers and the electron transport layers and, furthermore, reduced recombination centres in the perovskite films; these results in the enhanced photovoltaic properties. It has previously been reported that the fullerene layers can effectively passivate the charge trap states in perovskite and eliminate the hysteresis in PSCs.[54] *J-V* curves, shown in **Figure 4c**, indicate that the commonly observed hysteresis in c-TiO_2/m-TiO_2 PSCs is virtually negligible in the devices based on c-C_{60}/C_{60}-NPs.

The incident photon-to-electron conversion efficiency (IPCE) spectra of the PSCs based on different ETLs are dispalyed in **Figure 4d**. The integrated current densities calculated from the IPCE spectra are 21.41 and 22.19 mA cm^{-2} for solar cells based on c-TiO_2/m-TiO_2 and c-C_{60}/C_{60}-NPs, respectively. These are in good agreement with the J_{SC} values achieved from the *J-V* curves. **Figure 4e** shows the stabilised photocurrent density and power conversion efficiency at the maximum power point (0.89 V). A stable output efficiency of 19.37% was demonstrated. The performance reproducibility of OPSCs was studied by characterising 50 devices in the same batch. Histograms displaying the key parameters of these devices (**Figure 4e** and **Figure S6-S9**) indicate excellent reproducibility.

Owning to the photocatalytic activity of TiO_2, the ETL employing it tends to result in the degradation of PSCs under UV light.[55] Eliminating this unwanted effect is significant for the practical application of PSCs.[55] **Figure 5** presents the long-term stability studies of PSCs stored under three different aging conditions: i) under darkness

View Article Online
DOI: 10.1039/C8TA10510C

at 25 °C in 40% relative humidity without encapsulation; ii) under continuous UV illumination (1 mW cm^{-2}, λ= 365 nm) at 25 °C in 40% relative humidity without encapsulation; iii) under continuous full-sun illumination at the maximum power point tracking (MPPT) at 25 °C in 40% relative humidity with encapsulation. It can clearly be seen that, when stored under darkness, the PSCs based on C_{60}/C_{60}-NPs and c-TiO_2/m-TiO_2 both exhibit good long-term stability, maintaining over 90% of their initial performance after 1200 hours without encapsulation. However, when the unencapsulated devices were under exposure to 1 mW cm^{-2} UV illumination (λ= 365 nm), the PCE of the c-TiO_2/m-TiO_2 device decreases sharply and its performance is lost after 800 hours. According to the literature,[56,57] the drop-off in the performance of the TiO_2-based devices is mainly due to the intrisic UV instability of TiO_2. On the one hand, in the presence of UV light, photogenerated holes at the surface of TiO_2 react with oxygen absorbed at surface oxygen vacancies, and this results in an increased quantity of deep traps and an increase in the rate of charge recombination;[56] On the other hand, following UV-light exposure, electrons in the conduction band of TiO_2 can transform oxygen into hydroxyl radicals and the oxygen molecules absorbed on the TiO_2 trap states are likely to be reduced to HO· and H_2O, which promotes the degradation of the $MAPbI_3$ perovskite material.[57] In contrast, the c-C_{60}/C_{60}-NPs device aged under the same illumination and storing conditions maintains about 90% of its initial performance after 1200 hours, showing the outstanding UV stability of C_{60}/C_{60}-NPs devices. To further explore the potential of c-C_{60}/C_{60}-NPs devices, long-term lifetime of the encapsulated cells is recorded under continuous full-sun illumination at

View Article Online
DOI: 10.1039/C8TA10510C

a temperature of 25 °C in 40% relative humidity, where the maximum power output is tracked constantly. The test is applied to devices based on C_{60}/C_{60}-NPs and c-TiO_2/m-TiO_2, respectively, until the time at which 20% PCE (T_{80}) is lost. As shown in **Figure 5**, the PSCs based on c-TiO_2/m-TiO_2 ETL reached T_{80} after 85 hours of the applied stress test, while, in the same timeframe, the C_{60}/C_{60}-NPs-based PSC retained 98% of its initial PCE. In fact, the C_{60}/C_{60}-NPs-based PSC reached T_{80} after 720 h of continuous stress testing. The use of C_{60}/C_{60}-NPs ETL in PSCs showed a much stronger resistance to degradation during a much longer time period compared with devices based on c-TiO_2/m-TiO_2 ETL. This reveals that the organic scaffold is potentially the ideal material for electron collection layers to obtain both the highly efficient and long-term stable PSCs.

The room-temperature-processing organic scaffold enables the fabrication of flexible solar cells, and to demonstrate this, we fabricated the $MAPbI_3$ PSCs with the c-C_{60}/C_{60}-NPs ETL on ITO-coated polyethylene naphthalate (ITO/PEN) substrates. A digital photograph and schematic diagram of the final device are shown in **Figure 6a**. A flexible OPSC was therefore domenstrated for the first time with a PCE as high as 17.28%, which is one of the highest values among flexible $MAPbI_3$ solar cells (**Figure 6b**). The device performance of the best flexible OPSC, measured under different voltage scan direction, are summarised in the inset table in **Figure 6b**. The performance reproducibility of flexible OPSCs was studied by characterising 50 devices in the same batch. Histograms displaying the key parameters of these devices (**Figure S10-S13**) indicate excellent reproducibility. The average values of the device performance

View Article Online
DOI: 10.1039/C8TA10510C

calculated from 50 flexible OPSCs are presented in **Table 2**. To examine the stability of OPSCs against the mechanical bending, a bending test including 1000 consecutive bending cycles was carried out at two different radius of curvature (*R*) of 10 mm and 5 mm. When *R* was 10 mm, the flexible OPSCs exhibited no efficiency drop-off, maintaining 100% of its initial PCE after 1000 bending cycles, as domenstrated in **Figure 6c**. Furthermore, when *R* was 5 mm, the flexible OPSCs retained 95% of initial efficiency after 100 bending cycles, and maintained more than 90% of intial efficiency after 1000 cycles (**Figure 6c**). Therefore, these analyses demonstrate that our flexible OPSCs exhibit excellent stability under mechanical bending, indicating the great potential of OPSCs for practical applications.

In summary, we demonstrated a novel perovskite solar cell architecture based on room-temperature-processing single-crystalline C_{60} nanoparticles (C_{60}-NPs) serving as an efficient electron-selective layer. C_{60}-NPs, acting as a three-dimensional skeleton, improve the wettability between the C_{60} compact layer (c-C_{60}) and the precursor for the $MAPbI_3$ film, therefore enabling perovskite crystals to cover the substrate more uniformly and decrease the defect concentration of perovskite film. Moreover, compared to the conventionally-used electron-transport architecture c-TiO_2/m-TiO_2, the proposed organic scaffold architecture enhances electron transport and extraction and reduces charge accumulation at the interface. The organic-scaffold perovskite solar cells (OPSCs) achieved a highest PCE of 19.45%, outperforming standard reference PSCs based on c-TiO_2/m-TiO_2 (the highest PCE = 17.07%). Furthermore, c-C_{60}/C_{60}-NPs efficiently enhanced the UV stability of PSCs due to their inherent UV stability

View Article Online
DOI: 10.1039/C8TA10510C

compared to traditional c-TiO_2/m-TiO_2 ETLs. Most strikingly, the devices can be easily processed under low temperatures, offering an efficient method for the large-scale production of flexible PSCs. These flexible PSCs show remarkable performance with an excellent PCE of 17.28 % and good mechanical tolerance, which is among the highest values reported for flexible PSCs to date. This work reveals that organic nanostructures as n-type charge collection layers are excellent replacements for the inorganic mesoporous scaffold as they achieve remarkably high efficiency and long-term operational stability of both rigid and flexible perovskite solar cells.

View Article Online
DOI: 10.1039/C8TA10510C

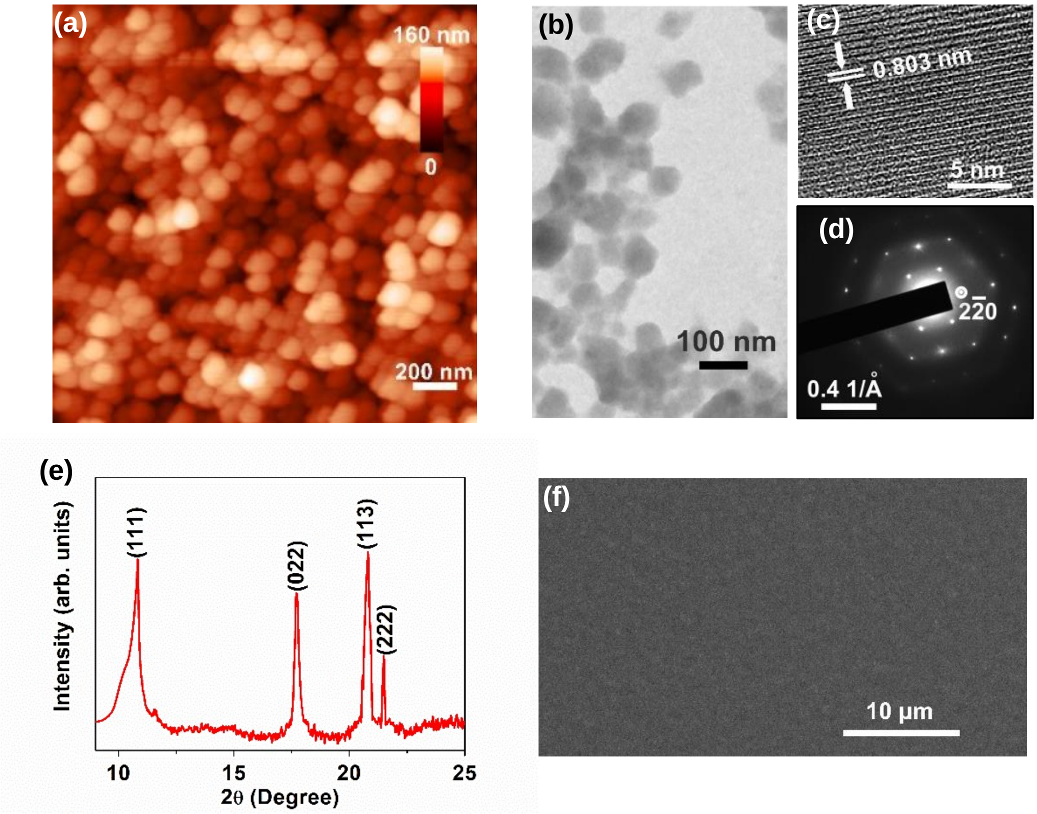

Figure 1 (a) AFM image of as-prepared C_{60} nanoparticles; (b) TEM image of C_{60} nanoparticles deposited on a copper mesh; (c) HRTEM image of C_{60} nanoparticles; (d) SAED pattern of C_{60} nanoparticles. Diffraction spot from the $(2\bar{2}0)$ plane is identified; (e) XRD pattern of C_{60} nanoparticles; (f) SEM image of C_{60} nanoparticles deposited on C_{60} compact layer.

.

View Article Online
DOI: 10.1039/C8TA10510C

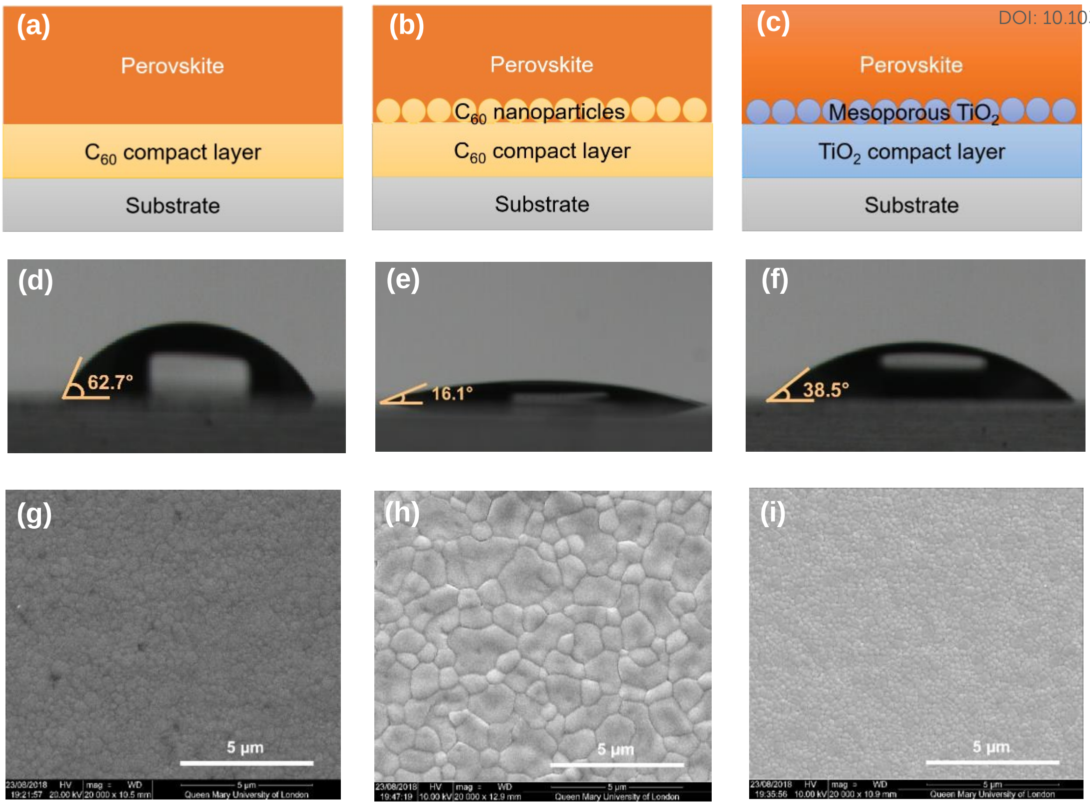

Figure 2 Schamatic diagram of perovskite deposited on (a) C_{60} compact layer, (b) C_{60}-NPs/c-C_{60} and (c) c-TiO_2/m-TiO_2; Perovskite precursor contact angles with (d) C_{60} compact layer, (e) C_{60}-NPs/c-C_{60} and (f) c-TiO_2/m-TiO_2; Top-view SEM images of the $MAPbI_3$ film deposited on (g) C_{60} compact layer, (h) C_{60}-NPs/c-C_{60} and (i) c-TiO_2/m-TiO_2.

View Article Online
DOI: 10.1039/C8TA10510C

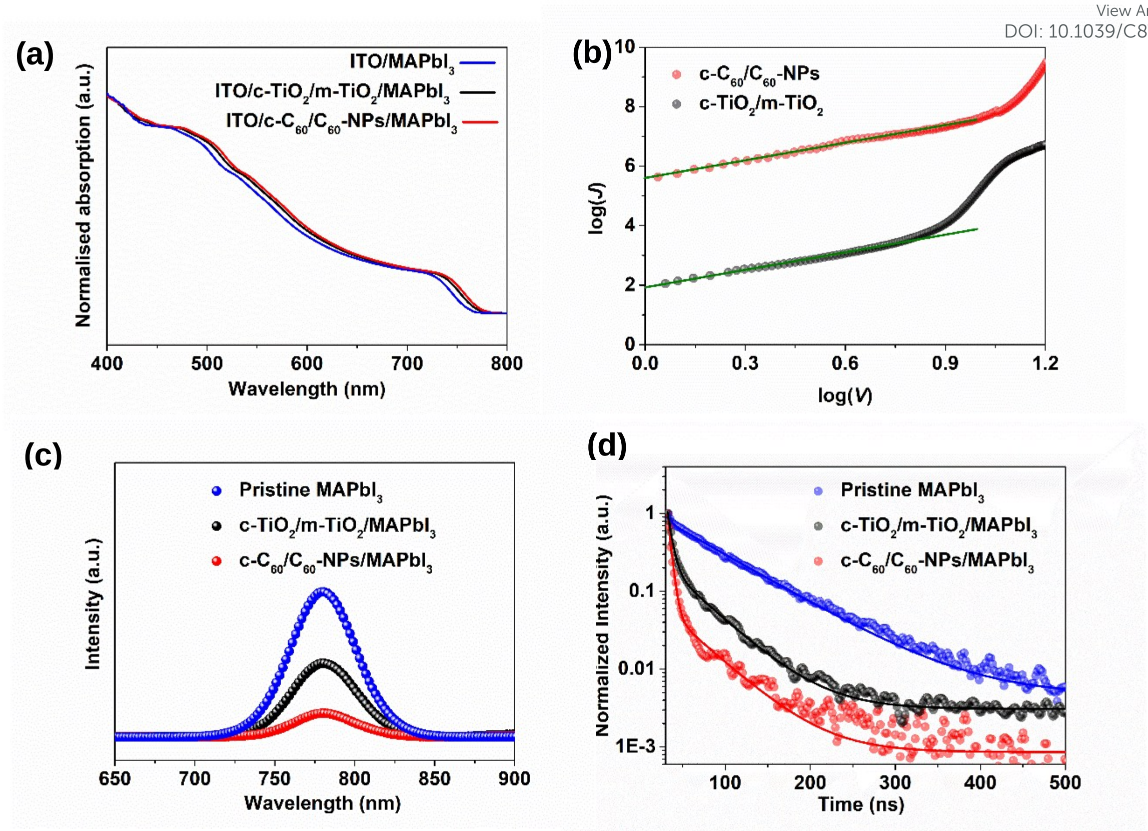

Figure 3 (a) UV-vis absorption spectra, (b) log(*J*)-log(*V*) plots, (c) steady-state PL spectra and (d) TRPL decay curves of perovskite films formed on ITO , ITO/c-C_{60}/C_{60}-NPs, and ITO/c-TiO_2/m-TiO_2, respectively.

View Article Online
DOI: 10.1039/C8TA10510C

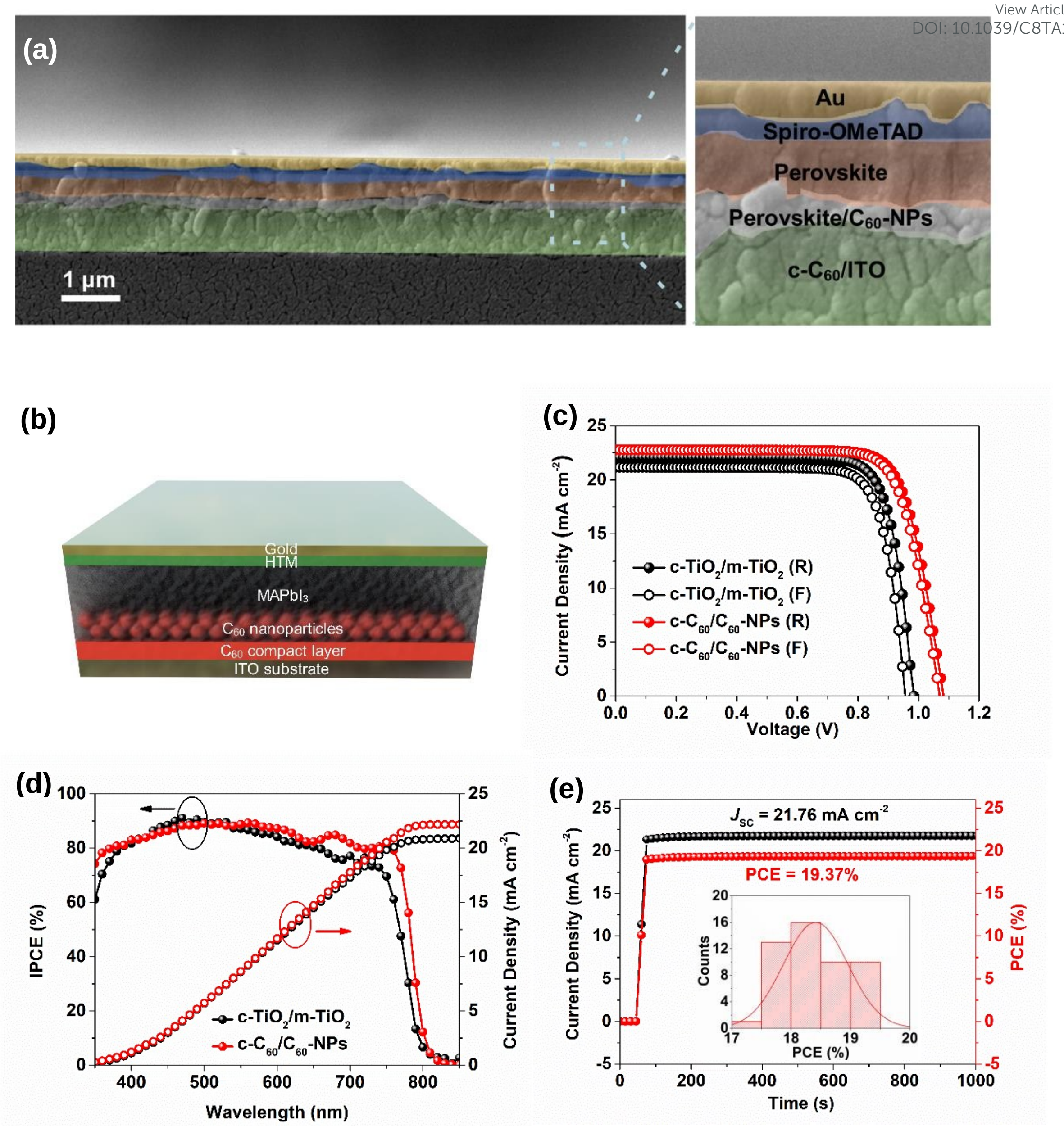

Figure 4 (a) Cross-sectional SEM image of the OPSC device containing a c-C_{60}/C_{60}-NP layer, (b) device configuration, (c) *J-V* characteristics and (d) IPCE spectra of the studied rigid PSCs using c-C_{60}/C_{60}-NPs and c-TiO_2/m-TiO_2, respectively; (e) The stabilized J_{SC} and PCE curves of PSCs using the c-C_{60}/C_{60}-NPs ETL measured under a constant bias of 0.89 V near the maximum power point and (inset) the histogram of rigid PSCs efficiencies.

View Article Online
DOI: 10.1039/C8TA10510C

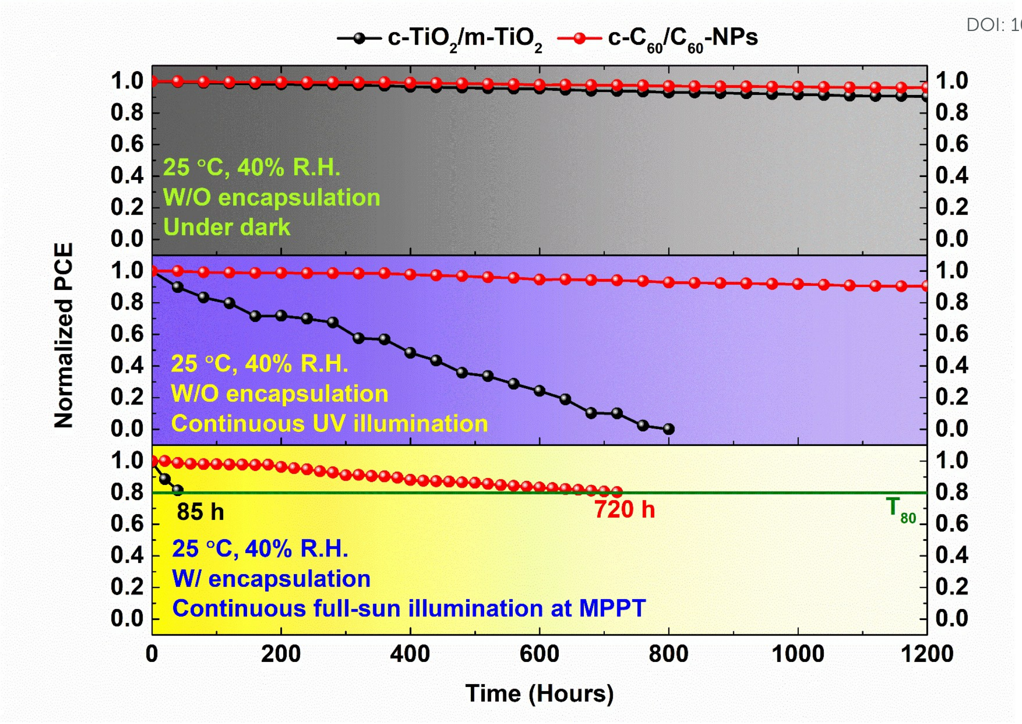

Figure 5 Long-term stability of the corresponding perovskite solar cells in three aging conditions: i) storing under dark at 25 °C in 40% relative humidity without encapsulation; ii) storing under continuous UV illumination (1 mW cm^{-2}, λ= 365 nm) at 25 °C in 40% relative humidity without encapsulation; iii) storing under continuous full-sun illumination at the maximum power point tracking (MPPT) at 25 °C in 40% relative humidity with encapsulation.

View Article Online
DOI: 10.1039/C8TA10510C

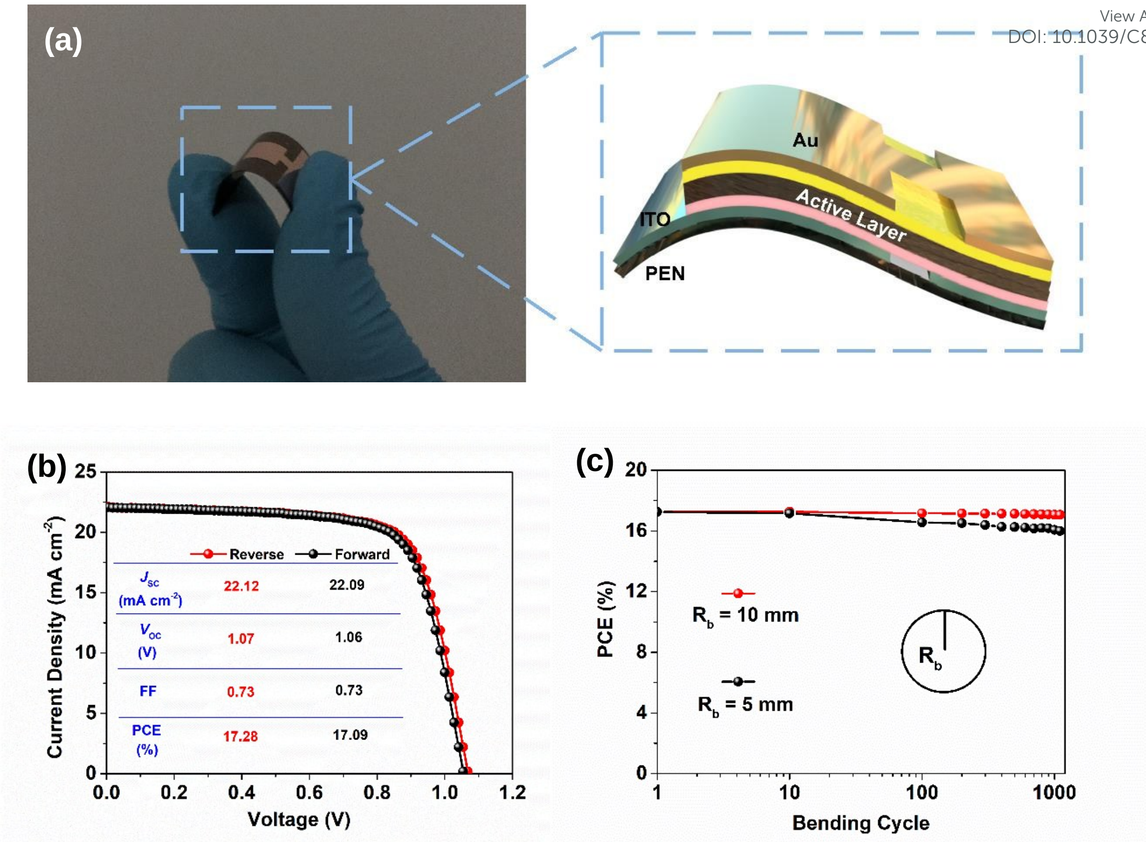

Figure 6 (a) A photograph and device configuration of a flexible $MAPbI_3$ OPSC on a PEN/ITO substrate; (b) *J-V* characteristics of a champion flexible OPSC; (c) PCE of flexible OPSCs as a function of bending cycles with different radius of curvature of 10 mm and 5 mm.

View Article Online
DOI: 10.1039/C8TA10510C

Table 1 Performance parameters of PSCs using different ETLs. Data were obtained by averaging 50 devices. The data in parentheses are for the best performing device.

ETL	Scan direction	J_{SC} (mA cm^{-2})	V_{oc} (V)	FF	PCE (%)
c-C_{60}/C_{60}-NPs	Reverse	22.33 ± 0.32 (22.79)	1.06 ± 0.02 (1.08)	0.78 ± 0.01 (0.79)	18.41 ± 0.54 (19.45)
	Forward	22.31 ± 0.36 (22.78)	1.05 ± 0.02 (1.07)	0.78 ± 0.01 (0.79)	18.29 ± 0.61 (19.26)
c-TiO_2/m-TiO_2	Reverse	21.73 ± 0.32 (22.10)	0.96 ± 0.02 (0.99)	0.75 ± 0.02 (0.78)	15.76 ± 0.61 (17.07)
	Forward	20.83 ± 0.36 (21.18)	0.92 ± 0.03 (0.96)	0.71 ± 0.03 (0.75)	15.16 ± 0.52 (15.25)

View Article Online
DOI: 10.1039/C8TA10510C

Table 2 Performance parameters of flexible PSCs based on organic scaffold. Data were obtained by averaging 50 devices. The data in parentheses are for the best performing device.

Scan direction	J_{SC} (mA cm^{-2})	V_{oc} (V)	FF	PCE (%)
Reverse	21.78 ± 0.31 (22.12)	1.05 ± 0.02 (1.07)	0.71 ± 0.03 (0.73)	16.71 ± 0.51 (17.28)
Forward	21.69 ± 0.36 (22.09)	1.04 ± 0.02 (1.06)	0.71 ± 0.02 (0.73)	16.59 ± 0.45 (17.09)

View Article Online
DOI: 10.1039/C8TA10510C

ASSOCIATED CONTENT

Supporting Information.

Experimental Section; Transmission spectrum of c-C_{60}/C_{60}-NPs and c-TiO_2/m-TiO_2 films deposited on a glass substrate; The structures of conventional perovskite solar cells with mesoporous TiO_2 and compact TiO_2 as an ETL; Key parameter metrics of PSCs based on different ELTs.

AUTHOR INFORMATION

Corresponding Author

*Email: Dr. Hongli Liu (email: liuhongli@tju.edu.cn); Prof. Shirong Wang (email: wangshirong@tju.edu.cn)

Author Contributions

The manuscript was written through contributions of all authors. All authors have given approval to the final version of the manuscript.

Notes

The authors declare no conflicts of interest.

ACKNOWLEDGMENT

View Article Online
DOI: 10.1039/C8TA10510C

This study was supported by the National Key R&D Program of China (2016YFB0401303), the National Nature Science Foundation of China (21676188) and the Key Projects in National Science Foundation of Tianjin (16JCZDJC37100).

View Article Online
DOI: 10.1039/C8TA10510C

REFERENCES

1 N. J. Jeon, H. Na, E. H. Jung, T. Y. Yang, Y. G. Lee, G. Kim, H. W. Shin, S. Il Seok, J. Lee and J. Seo, *Nat. Energy*, 2018, **3**, 682–689.

2 A. Kojima, K. Teshima, Y. Shirai and T. Miyasaka, *J. Am. Chem. Soc.*, 2009, **131**, 6050–6051.

3 W. S. Yang, B. W. Park, E. H. Jung, N. J. Jeon, Y. C. Kim, D. U. Lee, S. S. Shin, J. Seo, E. K. Kim, J. H. Noh and S. Il Seok, *Science (80-.).*, 2017, **356**, 1376–1379.

4 N. J. Jeon, J. H. Noh, Y. C. Kim, W. S. Yang, S. Ryu and S. Il Seok, *Nat. Mater.*, 2014, **13**, 897–903.

5 H. Zhou, Q. Chen, G. Li, S. Luo, T. -b. Song, H.-S. Duan, Z. Hong, J. You, Y. Liu and Y. Yang, *Science (80-.).*, 2014, **345**, 542–546.

6 N. J. Jeon, J. H. Noh, W. S. Yang, Y. C. Kim, S. Ryu, J. Seo and S. Il Seok, *Nature*, 2015, **517**, 476–480.

7 Y. Zhao, J. Wei, H. Li, Y. Yan, W. Zhou, D. Yu and Q. Zhao, *Nat. Commun.*, 2016, **7**, 10228.

8 X. Meng, X. Cui, M. Rager, S. Zhang, Z. Wang, J. Yu, Y. W. Harn, Z. Kang, B. K. Wagner, Y. Liu, C. Yu, J. Qiu and Z. Lin, *Nano Energy*, 2018, **52**, 123–133.

9 M. He, B. Li, X. Cui, B. Jiang, Y. He, Y. Chen, D. O'Neil, P. Szymanski, M. A. Ei-Sayed, J. Huang and Z. Lin, *Nat. Commun.*, 2017, **8**, 16045.

10 M. Ye, C. He, J. Iocozzia, X. Liu, X. Cui, X. Meng, M. Rager, X. Hong, X. Liu and Z. Lin, *J. Phys. D. Appl. Phys.*, 2017, 50, 373002.

DOI: 10.1039/C8TA10510C

11 M. He, X. Pang, X. Liu, B. Jiang, Y. He, H. Snaith and Z. Lin, *Angew. Chemie - Int. Ed.*, 2016, **55**, 4280–4284.

12 M. He, D. Zheng, M. Wang, C. Lin and Z. Lin, *J. Mater. Chem. A*, 2014, **2**, 5994–6003.

13 H. S. Kim, C. R. Lee, J. H. Im, K. B. Lee, T. Moehl, A. Marchioro, S. J. Moon, R. Humphry-Baker, J. H. Yum, J. E. Moser, M. Grätzel and N. G. Park, *Sci. Rep.*, 2012, **2**, 519.

14 J. Burschka, N. Pellet, S. J. Moon, R. Humphry-Baker, P. Gao, M. K. Nazeeruddin and M. Grätzel, *Nature*, 2013, **499**, 316–319.

15 M. M. Lee, J. Teuscher, T. Miyasaka, T. N. Murakami and H. J. Snaith, *Science (80-.).*, 2012, **338**, 643–647.

16 M. Liu, M. B. Johnston and H. J. Snaith, *Nature*, 2013, **501**, 395–398.

17 G. E. Eperon, V. M. Burlakov, P. Docampo, A. Goriely and H. J. Snaith, *Adv. Funct. Mater.*, 2014, **24**, 151–157.

18 C. V. Thompson, *Annu. Rev. Mater. Res.*, 2012, **42**, 399–434.

19 G. E. Eperon, S. N. Habisreutinger, T. Leijtens, B. J. Bruijnaers, J. J. Van Franeker, D. W. Dequilettes, S. Pathak, R. J. Sutton, G. Grancini, D. S. Ginger, R. A. J. Janssen, A. Petrozza and H. J. Snaith, *ACS Nano*, 2015, **9**, 9380–9393.

20 D. Bi, W. Tress, M. I. Dar, P. Gao, L. Jingshan, C. Renevier, K. Schenk, A. Abate, F. Giordano, J.-P. Correa-Baena, J.-D. Decoppet, S. M. Zakeeruddin, M. K. Nazeeruddin, M. Gratzel and A. Hagfeldt, *Sci. Adv.*, 2016, **2**, 1–7.

21 H. Tan, A. Jain, O. Voznyy, X. Lan, F. P. G. De Arquer, J. Z. Fan, R. Quintero-

View Article Online
DOI: 10.1039/C8TA10510C

Bermudez, M. Yuan, B. Zhang, Y. Zhao, F. Fan, P. Li, L. N. Quan, Y. Zhao, Z. H. Lu, Z. Yang, S. Hoogland and E. H. Sargent, *Science (80-.).*, 2017, **355**, 722–726.

22 M. Saliba, T. Matsui, K. Domanski, J. Y. Seo, A. Ummadisingu, S. M. Zakeeruddin, J. P. Correa-Baena, W. R. Tress, A. Abate, A. Hagfeldt and M. Gratzel, *Science (80-.).*, 2016, **354**, 206–209.

23 X. Li, D. Bi, C. Yi, J. D. Décoppet, J. Luo, S. M. Zakeeruddin, A. Hagfeldt and M. Grätzel, *Science (80-.).*, 2016, **353**, 58–62.

24 S. S. Shin, E. J. Yeom, W. S. Yang, S. Hur, M. G. Kim, J. Im, J. Seo, J. H. Noh and S. Il Seok, *Science (80-.).*, 2017, **356**, 167–171.

25 Y. K. Ren, X. H. Ding, Y. H. Wu, J. Zhu, T. Hayat, A. Alsaedi, Y. F. Xu, Z. Q. Li, S. F. Yang and S. Y. Dai, *J. Mater. Chem. A*, 2017, **5**, 20327–20333.

26 F. Zhang, W. Shi, J. Luo, N. Pellet, C. Yi, X. Li, X. Zhao, T. J. S. Dennis, X. Li, S. Wang, Y. Xiao, S. M. Zakeeruddin, D. Bi and M. Grätzel, *Adv. Mater.*, 2017, **29**, 1606806.

27 S. F. Völker, S. Collavini and J. L. Delgado, *ChemSusChem*, 2015, 8, 3012–3028.

28 C. Liu, Y. Yang, Y. Ding, J. Xu, X. Liu, B. Zhang, J. Yao, T. Hayat, A. Alsaedi and S. Dai, *ChemSusChem*, 2018, **11**, 1232–1237.

29 H. Yoon, S. M. Kang, J. K. Lee and M. Choi, *Energy Environ. Sci.*, 2016, **9**, 2262–2266.

30 S. Deguchi, S. A. Mukai, M. Tsudome and K. Horikoshi, *Adv. Mater.*, 2006, **18**, 729–732.

DOI: 10.1039/C8TA10510C

31 X. Zhao, T. Liu, Y. Cui, X. Hou, Z. Liu, X. Dai, J. Kong, W. Shi and T. J. S. Dennis, *Nanoscale*, 2018, **10**, 8170–8179.

32 X. Zhao, T. Liu, W. Shi, X. Hou, Z. Liu and T. J. S. Dennis, *J. Phys. Chem. C*, 2018, **122**, 8822–8828.

33 X. Zhao, T. Liu, X. Hou, Z. Liu, W. Shi and T. J. S. Dennis, *J. Mater. Chem. C*, 2018, **6**, 5489–5496.

34 X. Zhao, T. Liu, Y. Zhang, S. Wang, X. Li, Y. Xiao, X. Hou, Z. Liu, W. Shi and T. J. S. Dennis, *Adv. Mater. Interfaces*, 2018, **5**, 1800336.

35 X. Zhao, T. Liu, H. Liu, S. Wang, X. Li, Y. Zhang, X. Hou, Z. Liu, W. Shi and T. J. S. Dennis, *ACS Appl. Mater. Interfaces*, , DOI:10.1021/acsami.8b12832.

36 G. V. Andrievsky, M. V. Kosevich, O. M. Vovk, V. S. Shelkovsky and L. A. Vashchenko, *J. Chem. Soc. Chem. Commun.*, 1995, 1281–1282.

37 K. L. Chen and M. Elimelech, *Langmuir*, 2006, **22**, 10994–11001.

38 K. Miyazawa and Y. Kuwasaki, *J. Mater. Res.*, 2002, **17**, 83–88.

39 W. I. F. David, R. M. Ibberson, J. C. Matthewman, K. Prassides, T. J. S. Dennis, J. P. Hare, H. W. Kroto, R. Taylor and D. R. M. Walton, *Nature*, 1991, **353**, 147–149.

40 X. Liu, C. C. Chueh, Z. Zhu, S. B. Jo, Y. Sun and A. K. Y. Jen, *J. Mater. Chem. A*, 2016, **4**, 15294–15301.

41 M. Ramesh, K. M. Boopathi, T. Y. Huang, Y. C. Huang, C. S. Tsao and C. W. Chu, *ACS Appl. Mater. Interfaces*, 2015, **7**, 2359–2366.

42 S. Roy, D. Bandyopadhyay, A. Karim and R. Mukherjee, *Macromolecules*, 2015,

View Article Online
DOI: 10.1039/C8TA10510C

48, 373–382.

43 S. Sharma, M. H. Rafailovich, D. Peiffer and J. Sokolov, *Nano Lett.*, 2001, **1**, 511–514.

44 R. S. Krishnan, M. E. Mackay, P. M. Duxbury, C. J. Hawker, S. Asokan, M. S. Wong, R. Goyette and P. Thiyagarajan, *J. Phys. Condens. Matter*, 2007, **19**, 356003.

45 R. Kanemoto, A. Anas, Y. Matsumoto, R. Ueji, T. Itoh, Y. Baba, S. Nakanishi, M. Ishikawa and V. Biju, *J. Phys. Chem. C*, 2008, **112**, 8184–8191.

46 Q. Jiang, L. Zhang, H. Wang, X. Yang, J. Meng, H. Liu, Z. Yin, J. Wu, X. Zhang and J. You, *Nat. Energy*, 2016, **2**, 16177.

47 Y. Li, Y. Zhao, Q. Chen, Y. Yang, Y. Liu, Z. Hong, Z. Liu, Y. T. Hsieh, L. Meng, Y. Li and Y. Yang, *J. Am. Chem. Soc.*, 2015, **137**, 15540–15547.

48 A. E. Shalan, T. Oshikiri, S. Narra, M. M. Elshanawany, K. Ueno, H. P. Wu, K. Nakamura, X. Shi, E. W. G. Diau and H. Misawa, *ACS Appl. Mater. Interfaces*, 2016, **8**, 33592–33600.

49 F. Zhang, D. Bi, N. Pellet, C. Xiao, Z. Li, J. J. Berry, S. M. Zakeeruddin, K. Zhu and M. Grätzel, *Energy Environ. Sci.*, , DOI:10.1039/C8EE02252F.

50 J. Feng, X. Zhu, Z. Yang, X. Zhang, J. Niu, Z. Wang, S. Zuo, S. Priya, S. Liu and D. Yang, *Adv. Mater.*, 2018, **30**, 1801418.

51 J. H. Heo, D. H. Song, H. J. Han, S. Y. Kim, J. H. Kim, D. Kim, H. W. Shin, T. K. Ahn, C. Wolf, T. W. Lee and S. H. Im, *Adv. Mater.*, 2015, **27**, 3424–3430.

52 X. Li, J. Yang, Q. Jiang, H. Lai, S. Li, J. Xin, W. Chu and J. Hou, *ACS Nano*,

View Article Online
DOI: 10.1039/C8TA10510C

2018, **12**, 5605–5614.

53 M. Ulfa, T. Zhu, F. Goubard and T. Pauporté, *J. Mater. Chem. A*, 2018, **6**, 13350–13358.

54 Y. Shao, Z. Xiao, C. Bi, Y. Yuan and J. Huang, *Nat. Commun.*, 2014, **5**, 5784.

55 M. M. Tavakoli, F. Giordano, S. M. Zakeeruddin and M. Grätzel, *Nano Lett.*, 2018, **18**, 2428–2434.

56 T. Leijtens, G. E. Eperon, S. Pathak, A. Abate, M. M. Lee and H. J. Snaith, *Nat. Commun.*, 2013, **4**, 2885.

57 W. Li, J. Li, G. Niu and L. Wang, *J. Mater. Chem. A*, 2016, **4**, 11688–11695.

Graphical Abstract

View Article Online
DOI: 10.1039/C8TA10510C

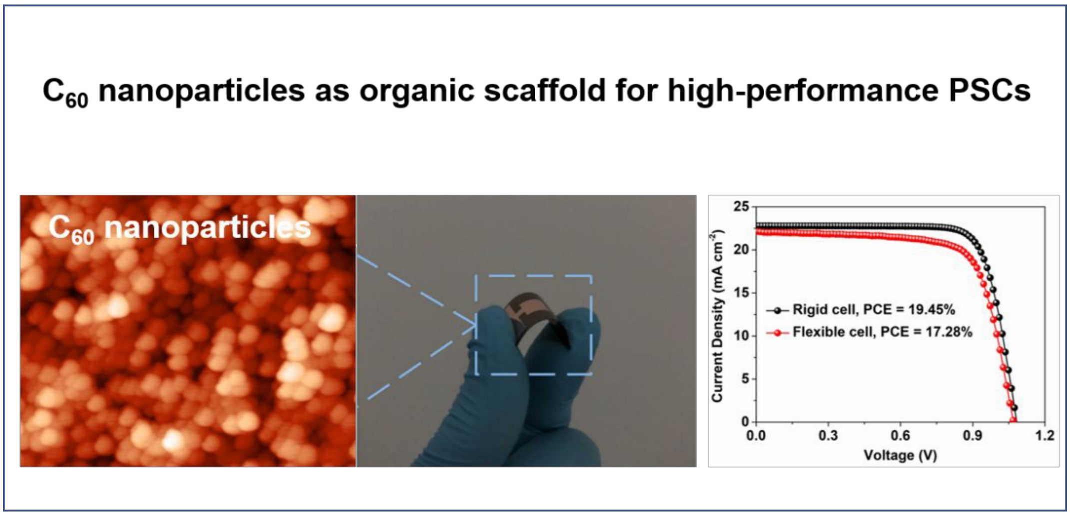

Room-temperature-processing C_{60} single-crystalline nanoparticles were employed as high-performance organic electron-selective scaffold for both rigid and flexible perovskite solar cells.